The Astrophysical Journal, 924:75 (16pp), 2022 January 10 https://doi.org/10.3847/1538-4357/ac34f6

Convection and Dynamo in Newly Born Neutron Stars

Youhei Masada[1], Tomoya Takiwaki[2], and Kei Kotake[3]
[1] Department of Science Education, Aichi University of Education, Kariya 448-8542, Japan; ymasada@auecc.aichi-edu.ac.jp
[2] Division of Science, National Astronomical Observatory of Japan, Tokyo 181-8588, Japan
[3] Faculty of Science, Department of Applied Physics & Research Institute of Stellar Explosive Phenomena, Fukuoka University, Fukuoka 814-0180, Japan
Received 2021 October 9; revised 2021 October 26; accepted 2021 October 28; published 2022 January 13

Abstract

To study properties of magnetohydrodynamic (MHD) convection and resultant dynamo activities in proto-neutron stars (PNSs), we construct a "PNS in a box" simulation model and solve the compressible MHD equation coupled with a nuclear equation of state (EOS) and simplified leptonic transport. As a demonstration, we apply it to two types of PNS model with different internal structures: a fully convective model and a spherical-shell convection model. By varying the spin rate of the models, the rotational dependence of convection and the dynamo that operate inside the PNS is investigated. We find that, as a consequence of turbulent transport by rotating stratified convection, large-scale structures of flow and thermodynamic fields are developed in all models. Depending on the spin rate and the depth of the convection zone, various profiles of the large-scale structures are obtained, which can be physically understood as steady-state solutions to the "mean-field" equation of motion. Additionally to those hydrodynamic structures, a large-scale magnetic component of $\mathcal{O}(10^{15})$ G is also spontaneously organized in disordered tangled magnetic fields in all models. The higher the spin rate, the stronger the large-scale magnetic component grows. Intriguingly, as an overall trend, the fully convective models have a stronger large-scale magnetic component than that in the spherical-shell convection models. The deeper the convection zone extends, the larger the size of the convective eddies becomes. As a result, rotationally constrained convection seems to be more easily achieved in the fully convective model, resulting in a higher efficiency of the large-scale dynamo there. To gain a better understanding of the origin of the diversity of a neutron star's magnetic field, we need to study the PNS dynamo in a wider parameter range.

Unified Astronomy Thesaurus concepts: Magnetohydrodynamics (1964); Core-collapse supernovae (304); Astrophysical fluid dynamics (101); Plasma astrophysics (1261); Magnetohydrodynamical simulations (1966)

1. Introduction

Neutron stars (NSs) have the most extreme magnetic fields in the universe, typically a trillion, and up to a quadrillion times more powerful than Earth's. Although we know that they are formed in the aftermath of massive stellar core-collapse, the origin of the magnetic field is still an outstanding issue in astrophysics. Mainly, two possible origins have been proposed: the fossil field and dynamo field hypotheses (e.g., Spruit 2008; Ferrario et al. 2015). While the former regards the field as an inheritance from the NS's main-sequence progenitor (e.g., Ruderman 1972), the latter presumes that it would be generated by some dynamo processes in newly born NSs, also known as proto-neutron stars (PNSs) (e.g., Ruderman & Sutherland 1973; Thompson & Duncan 1993, hereafter TD93). Here the PNS is conventionally defined as a lepton-rich core inside a pseudo-surface with a density of $\rho = 10^{11}$ g cm^{-3} (e.g., Morozova et al. 2018; Torres-Forné et al. 2018).

One important physical process, which should be examined further in either scenarios, is the role of PNS convection. Even if a strong fossil field exists before the collapse, it should be subjected to vigorous convective motions after the formation of the PNS (e.g., Epstein 1979; Burrows & Lattimer 1988; Keil et al. 1996). It is not fully discussed whether the structure and coherence of the fossil magnetic field are retained in such a tumultuous situation. At least, independent from the spin rate of the PNS, the turbulent convection would strongly disturb, locally amplify, and transport the fossil field (Nordlund et al. 1994), unless the field strength is greater than the equipartitioned one. The characteristics of the fossil field acquired before core-collapse thus seem likely to be lost during the evolution of the PNS. On the flip side, in the dynamo hypothesis, the convective motion would play a vital role in generating the large-scale magnetic field in the PNS. Its importance is indisputable.

The convective dynamo in the PNS is discussed in TD93 theoretically under the modern scenario of the core-collapse supernova. In the context of the α–Ω dynamo (e.g., Parker 1955), they argue that a large-scale magnetic field of $\mathcal{O}(10^{15})$ G is generated when the spin period of the PNS ($\equiv P_{\rm rot}$) is shorter than $\mathcal{O}(10)$ ms. This constraint comes from the prerequisite for operating the large-scale convective dynamo (e.g., Moffatt 1978; Krause & Raedler 1980): *the Rossby number should be smaller than unity*, that is, $Ro \equiv v/(2\Omega l) \lesssim 1$, where the spin rate is Ω, and the typical velocity v and length scale l with their chosen values $v \simeq \mathcal{O}(10^3)$ km s^{-1} and $l \simeq \mathcal{O}(0.1)$ km correspond to the convection velocity and scale height expected in the outer region of the PNS. In an ordinary PNS with $P_{\rm rot} \gtrsim \mathcal{O}(10)$ ms (e.g., Ott et al. 2006), the large-scale magnetic field does not grow and small-scale "patchy" magnetic structures would prevail. This is the standard, but still rough, framework they constructed for the PNS dynamo.

Numerical modeling is a powerful tool to refine the PNS dynamo theory. Bonanno et al. (2003) were the first to study the dynamo process in the PNS in the framework of the mean-field approximation. They solved a mean-field induction equation with given profiles of turbulent electromotive force and differential rotation without solving the development of the flow field. Then, they showed that the mean-field dynamo process would be effective for most of the PNS (see also Bonanno et al. 2006). Rheinhardt & Geppert (2005) studied the ability of PNS convection to excite the dynamo, considering actual convection profiles taken from hydrodynamic simulations of rotating PNSs, and then showed that the geometrical structures of the velocity fields they employed are well suited to amplify a seed magnetic field. More recently, a groundbreaking study of the PNS dynamo was conducted by Raynaud et al. (2020). They performed anelastic MHD simulations of the PNS dynamo under a realistic setup and then confirmed, for the fist time, that the large-scale convective dynamo successfully occurs in a rapidly rotating PNS, as predicted by TD93.

Although significant progress has been made in the study of the PNS dynamo with the development of the numerical method and improved computing performance, the origin of the diversity of NSs' magnetic fields remains to be solved. "What physics is responsible for the diversity of NSs' magnetic fields?" To answer this question, we join the effort in numerical modeling of the PNS dynamo. The aim of our study is to give shape to the theory of the PNS convection and dynamo in a more quantitative, self-consistent manner with the aid of numerical simulation. As a first step toward it, we construct a "PNS in a box" simulation model, solving the compressible MHD with a nuclear equation of state (EOS) and a simplified leptonic transport process. Our simulation model is able to study various types of PNS structure from spherical-shell convection states to a full-sphere convection state. As a demonstration of our newly developed model, here we study convection and dynamo processes in two types of PNSs with different internal structure: one is in a fully convective state and the other has a spherical-shell convection state. The internal structures of the PNS models are taken from core-collapse simulations, and thus are more or less realistic. The dependence of the properties of the PNS dynamo on the spin rate is also studied by varying it systematically.

The outline of this paper is as follows. In Section 2 we present the numerical model we constructed and the simulation setups. The results obtained from the simulation run for models with different depths of the convection zone (CZ) and various spin rates are presented in Section 3, with special focus on the profiles of large-scale fields developed in models. The spin rate dependence of the dynamo activity and its relationship with the turbulent electromotive force are discussed in Section 4. We summarize and discuss the implications of our results in Section 5.

2. Simulation Model

It is well known that the width of the CZ in the PNS changes depending not only on the physical properties of the progenitor star (e.g., Nagakura et al. 2020; Torres-Forné et al. 2019) but also on the evolutionary phase of the PNS (e.g., Keil et al. 1996; Pons et al. 1999; Roberts et al. 2012; Camelio et al. 2019). Since CZs with various depths are expected to develop in the interior of the PNS, the numerical model should be able to examine them comprehensively. To understand the origin of the diversity of the NS's magnetic fields, we construct a kind of "star in a box" simulation model (Freytag et al. 2002; Dobler et al. 2006; Käpylä 2021).

To cover the whole sphere from the center to the pseudo-surface, the PNS is described as a spherical subregion of radius $R_{\rm PNS}$ of a cubic box of size $L_{\rm box}^3$ and is solved in the Cartesian grid (x, y, z). The spherical coordinates (r, θ, ϕ) are used for analysis. The baryonic matter in the box is governed by fully compressible nonrelativistic MHD equations. General relativistic effects are not taken into consideration in this work. The leptonic transport that characterizes the PNS is additionally solved under the diffusion approximation. The basic equations are written, in a rotating reference frame with an angular velocity Ω_0, as

$$\frac{D\rho}{Dt} + \rho\nabla\cdot\boldsymbol{v} = 0, \tag{1}$$

$$\frac{D\boldsymbol{v}}{Dt} = -2\Omega_0\boldsymbol{e}_z\times\boldsymbol{v} - \frac{1}{\rho}\nabla P + \frac{1}{4\pi\rho}(\nabla\times\boldsymbol{B})\times\boldsymbol{B} + \frac{2}{\rho}\nabla\cdot(\rho\nu\boldsymbol{S}) + \boldsymbol{g} + \boldsymbol{f}_{\rm damp}, \tag{2}$$

$$\frac{D\epsilon}{Dt} = -\frac{P\nabla\cdot\boldsymbol{v}}{\rho} + 2\nu\boldsymbol{S}^2 + \frac{\eta(\nabla\times\boldsymbol{B})^2}{4\pi\rho} + \frac{\gamma\nabla\cdot(\kappa\nabla\epsilon)}{\rho} + \dot{\epsilon}_{\rm damp}, \tag{3}$$

$$\frac{\partial\boldsymbol{B}}{\partial t} = \nabla\times(\boldsymbol{v}\times\boldsymbol{B} - \eta\nabla\times\boldsymbol{B}), \tag{4}$$

$$\frac{DY_e}{Dt} = \nabla\cdot(\xi\nabla Y_e) + \dot{Y}_{e,\rm source}, \tag{5}$$

with the strain rate tensor

$$S_{ij} \equiv (\partial_j v_i + \partial_i v_j - 2\delta_{ij}\partial_i v_i/3)/2, \tag{6}$$

where ϵ is the specific internal energy, Y_e is the lepton fraction, γ is the adiabatic index, and the other symbols have their usual meanings. The viscous, magnetic, heat, and lepton diffusivities are given by ν, η, κ, and ξ, respectively. To avoid boundary artifacts, the damping terms $\boldsymbol{f}_{\rm damp}$ and $\dot{\epsilon}_{\rm damp}$ are added to Equations (2) and (3), which keep $\boldsymbol{v}$ and ϵ outside the PNS close to the initial profiles, and are given by

$$\boldsymbol{f}_{\rm damp} = -\frac{\boldsymbol{v}}{\tau_d}f_{\rm ext}\,,\ \dot{\epsilon}_{\rm damp} = \frac{\epsilon_{\rm ini}-\epsilon}{\tau_d}f_{\rm ext}\,, \tag{7}$$

with

$$f_{\rm ext} = \frac{1}{2}\left[1 + \tanh\left(\frac{r-R_d}{w_t}\right)\right], \tag{8}$$

where $\epsilon_{\rm ini}$ is the initial profile of ϵ, R_d is the damping radius, τ_d is the damping time, and w_t is the width of the transition layer between the PNS and the "buffer" damping region. To maintain the lepton gradient, the source term is added to the lepton transport equation,

$$\dot{Y}_{e,\rm source} = \frac{Y_{e,\rm ini}-Y_e}{\tau_s}f_{\rm int} \tag{9}$$

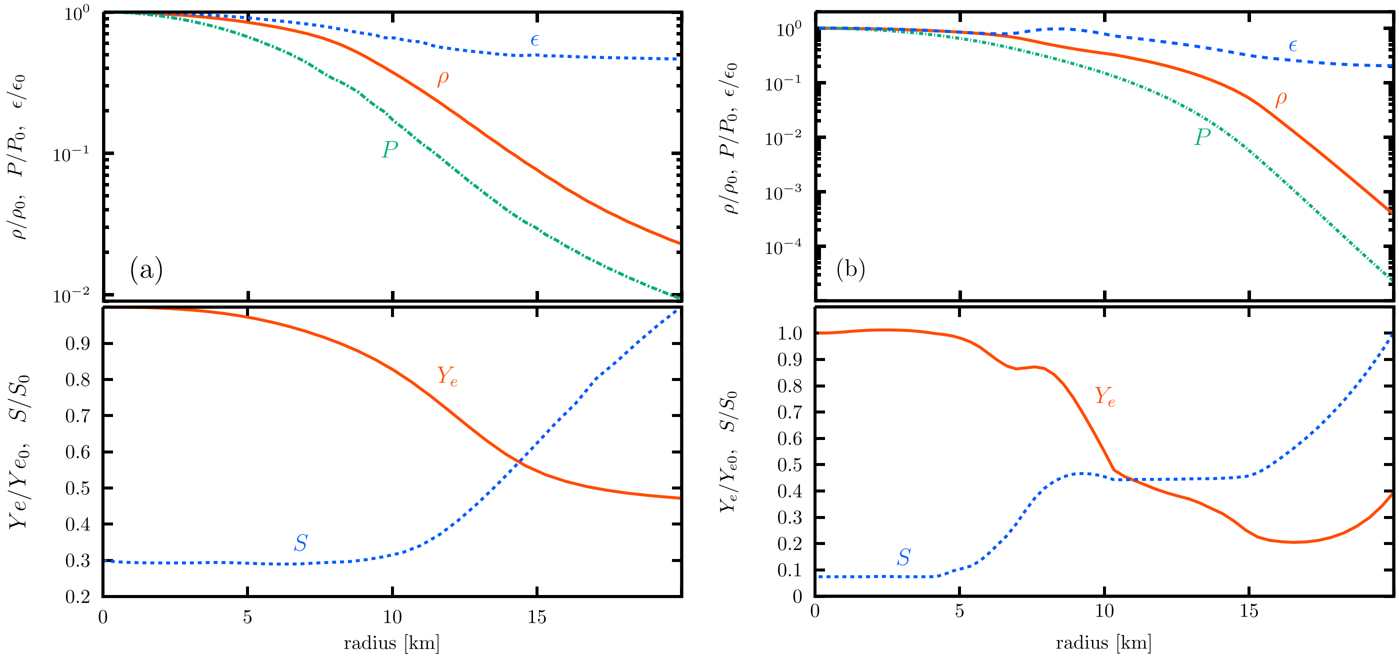

Figure 1. Radial distributions of ρ, P, ϵ (top), and Y_e, S (bottom) for (a) full-sphere convection model (model mf) and (b) spherical-shell convection model (model ms). Normalizations are $\rho_0 = 2.5 \times 10^{14}$ g cm^{-3}, $P_0 = 5.86 \times 10^{33}$ dyn cm^{-2}, $\epsilon_0 = 5.85 \times 10^{19}$ erg g^{-1}, $Y_{e0} = 0.35$, and $S_0 = 3.96 k_{\rm B}$ for model mf, $\rho_0 = 6.23 \times 10^{14}$ g cm^{-3}, $P_0 = 5.54 \times 10^{34}$ dyn cm^{-2}, $\epsilon_0 = 8.15 \times 10^{20}$ erg g^{-1}, $Y_{e0} = 0.27$, and $S_0 = 6.51 k_{\rm B}$ for model ms.

with

$$f_{\rm int} = \frac{1}{2}\left[1 - \tanh\left(\frac{r - R_d}{w_t}\right)\right], \tag{10}$$

where $Y_{e,\rm ini}$ is the initial profile of Y_e, and τ_s is the forcing time. This is a simple model for replenishment of the leptons via energy conversion from gravity to neutrino radiation inside the PNS during its cooling time.[4] To close the system, we employ the EOS by Lattimer & Swesty (1991) with a compressibility modulus of $K = 220$ MeV.

We set up two types of initial equilibrium model as typical examples for our newly developed code: model mf is based on a post-bounce core (about 100 ms after the core bounce) from a hydrodynamic simulation of "rotating" core-collapse of a 15 $M_\odot$ progenitor, and model ms is based on a post-bounce core (about 600 ms after the bounce) of "nonrotating" core-collapse of an 11.2 $M_\odot$ progenitor. In both models, the shock wave has reached ∼200 km, and the PNSs are settled into a quasi-hydrostatic state. The hydrodynamic variables and gravitational potential within $0 \leqslant r \leqslant 20$ km ($\equiv L_{\rm box}/2$) are extracted, and then the PNS is reconstructed with a second-order interpolation method in the range of the calculation domain $-L_{\rm box}/2 \leqslant x, y, z \leqslant L_{\rm box}/2$.

Shown in Figure 1 is the initial profile of the hydrodynamic variables for (a) model mf and (b) model ms. The profiles of ρ, P, and ϵ are shown in the top panels, and Y_e and S (entropy) in the bottom panels. The radial profile of the density scale height H_ρ for each model is also shown in Figure 2. There is no significant difference in the profile of H_ρ between the two models. However, there are remarkable differences in the profiles of Y_e and S. For model mf, while the negative lepton gradient that lies in the inner part of the PNS powers the lepton-driven convection (e.g., Epstein 1979; Keil et al. 1996), the outer region where $r \gtrsim 15$ km is stable to the convective instability based on the Ledoux criterion (e.g., Ledoux 1947; Kippenhahn & Weigert 1990). In contrast, for model ms, the possible site for the lepton-driven convection is confined to the layer in the range 7.5 km $\lesssim r \lesssim$ 15 km, while the inner core and outer envelope are convectively stable due to the positive entropy gradient. In this paper, to explore the response of the PNS convection and dynamo to the spin rate, we vary the magnitude of Ω_0 in two models while keeping the background hydrostatic state unchanged. We investigate the cases with $\Omega_0 = 12\pi$, 60π, and 120π rad s^{-1} for model mf and the cases with $\Omega_0 = 100\pi$, 300π, and 900π rad s^{-1} for model ms. See the summary of the simulation run in Table 1.

Since the outer convectively stable layer has less impact on the hydrodynamics of the PNS during the evolution time of

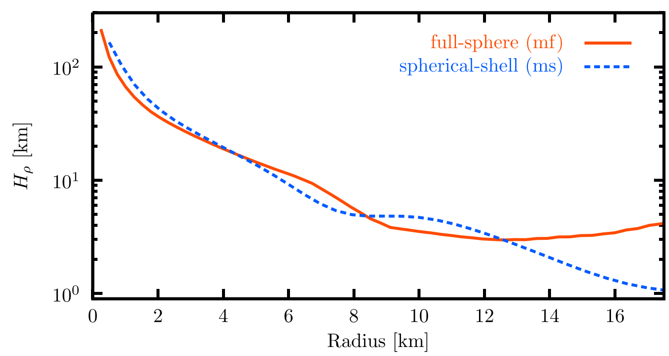

Figure 2. Radial distribution of the density scale height ($H_\rho \equiv -dr/d\ln\rho$) for model mf (red solid curve) and model ms (blue dashed curve).

[4] Our PNS dynamo simulations focus on timescales of less than "300 ms", which is shorter than the typical thermodynamic evolution time of the PNS (e.g., ∼1000 ms in Scheck et al. 2006 for the standard case). On such a timescale, the behavior of neutrino transport is expected to be similar to (not so different from) that in the condition adopted as our initial setup. Hence, we model lepton-driven convection by adding the forcing term, which can maintain the initial profile of the lepton fraction moderately, to the lepton transport equation.

Table 1
Summary of the Simulation Runs

	Ω_0 [rad s^{-1}]	R_d [km]	$v_{\rm mean}$ [km s^{-1}]	$Ro_{\rm mean}$	$\langle\epsilon_{\rm K}\rangle$ [erg cm^{-3}]	$\langle\epsilon_{\rm M}\rangle$ [erg cm^{-3}]	$\epsilon_{\rm Mm}^{l=1-3}$ [erg cm^{-3}]
mf12p	12π	17.5	9.2×10^2	0.81	3.7×10^{30}	9.6×10^{29}	2.5×10^{25}
mf60p	60π	17.5	7.5×10^2	0.13	3.0×10^{30}	8.9×10^{29}	5.8×10^{26}
mf120p	120π	17.5	6.7×10^2	0.06	3.0×10^{30}	8.1×10^{29}	4.1×10^{27}
ms100p	100π	17.0	2.2×10^3	0.50	6.8×10^{30}	1.5×10^{30}	3.8×10^{25}
ms300p	300π	17.0	2.0×10^3	0.15	5.8×10^{30}	1.3×10^{30}	5.5×10^{25}
ms900p	900π	17.0	2.0×10^3	0.05	4.7×10^{30}	1.2×10^{30}	1.1×10^{26}

Note. The models with prefixes mf and ms correspond to the models with the full-sphere CZ and spherical-shell CZ. The mean quantities $v_{\rm mean}$, $Ro_{\rm mean}$, $\langle\epsilon_{\rm M}\rangle$, $\langle\epsilon_{\rm K}\rangle$ are evaluated at the saturated state, where $v_{\rm mean}\equiv\langle\langle(v_r-\langle\langle v_r\rangle_\phi\rangle)^2\rangle_{\rm V}^{1/2}\rangle$ and $Ro_{\rm mean}\equiv v_{\rm mean}/(2\Omega_0 w_{\rm cz})$ with the width of the CZ, $w_{\rm cz}$, for each model, mf ($w_{\rm cz}=15$ km) or mf ($w_{\rm cz}=7$ km).

interest ($\mathcal{O}(100)$ ms), the damping radius is chosen as $R_d=17.5$ km so that the pseudo-surface of the PNS would be $R_{\rm PNS}\simeq15$ km. We connect the PNS to the outer buffer region through the transition layer with $w_t=0.05R_{\rm PNS}$. The forcing time for the lepton is assumed to be constant inside the PNS and an order of magnitude shorter than the typical convective turnover time, that is $\tau_s=0.1\tau_{\rm cv}$, where $\tau_{\rm cv}\equiv l_{\rm sh}/v_{\rm cv}$ with the typical convection velocity $v_{\rm cv}=10^8$ cm s^{-1} and the typical scale height $l_{\rm sh}=10^5$ cm. With this value, we can keep the profile of Y_e close to, but slightly deviating from, the initial state. To reduce the boundary artifacts as much as possible, we adopt a short damping time of $\tau_d=0.1\tau_s$. We choose, as a first step, uniform diffusivities of $\nu=\eta=\kappa=\xi=10^{11}$ cm^2 s^{-1} inside the PNS. While ν, κ, and ξ assumed here are within the expectations in the PNS[5], η is far from a realistic value ($\eta_{\rm PNS}\sim10^{-5}$ cm^2 s^{-1}) (e.g., Rheinhardt & Geppert 2005; Masada et al. 2007) because of a numerical limitation, as is so often the case with the planetary and stellar dynamo simulations (e.g., Jones 2011; Brun & Browning 2017).

The governing equations are solved by the second-order Godunov-type finite-difference scheme, which employs an approximate MHD Riemann solver (see Sano et al. 1999; Masada et al. 2012, 2015, for details). The calculation domain is resolved into $N^3=256^3$ grid points. After a random small "seed" magnetic field with amplitude $|\delta B|<10^9$ G is introduced into the CZ of the PNS, the calculation is started by adding a small perturbation to the initial pressure distribution for both models. Note that, in this paper, the simulation is terminated when the calculation time exceeds roughly 250 ms, taking into account that the structure of the PNS can change in about a few hundred milliseconds as the neutrino radiation proceeds (e.g., Keil et al. 1996; Scheck et al. 2006; Nagakura et al. 2020).

In the following, to examine the convective and magnetic structures in detail, we define the following three averages of an arbitrary function $h(r, \theta, \phi)$.[6]

1. The volume average over the entire CZ:
$$\langle h\rangle_{\rm V}\equiv\int h(r,\theta,\phi)dV_{\rm cz}\Big/\int dV_{\rm cz},\tag{11}$$
where $V_{\rm cz}$ is the volume of the CZ.
2. The longitudinal average:
$$\langle h\rangle_\phi=\frac{1}{2\pi}\int_{-\pi}^{\pi}h(r,\theta,\phi)d\phi.\tag{12}$$
3. The spherical average:
$$\langle h\rangle_s=\frac{1}{4\pi}\int_{-1}^{1}\int_{-\pi}^{\pi}h(r,\theta,\phi)d\cos\theta d\phi.\tag{13}$$

The time average of each spatial mean is denoted by additional angular brackets, such as $\langle\langle h\rangle_\theta\rangle$.

3. Results

3.1. Temporal Evolution and Convection Profiles

The rough sketch of the simulation results is summarized. The typical temporal evolution of the volume-averaged kinetic and magnetic energies ($\epsilon_{\rm K}$ and $\epsilon_{\rm M}$) for (a) model mf (mf12p) and (b) model ms (ms100p) is shown in Figure 3, where $\epsilon_{\rm K}\equiv\langle\rho\boldsymbol{v}^2/2\rangle_{\rm V}$ and $\epsilon_{\rm M}\equiv\langle\boldsymbol{B}^2/(8\pi)\rangle_{\rm V}$. The volume average is taken over the entire CZ. When the simulation proceeds, the lepton-driven convection begins to grow and then both kinetic and magnetic energies are amplified in the PNS. The kinetic energy saturates within ∼50 ms. At the saturated stage, the turbulent convective motion dominates the PNS as shown in Figure 4, where the structure of the convection on the PNS surface (left hemisphere) and on the meridional cutting plane (right hemisphere) for model mf (mf12p) is visualized as a demonstration. In contrast, the magnetic energy gradually increases and reaches a quasi-steady state after $t=150$–200 ms in both models. Since the convective turnover time is longer in models mf than in models ms due to the larger scale height in the deeper CZ, it takes a longer time for the magnetic energy to be amplified. The saturation level of the magnetic energy is below that of the convective kinetic energy, suggesting that the MHD dynamos operated in our models are in a turbulent regime rather than a magnetostrophic regime (e.g., Brun &

[5] In the PNS below the neutrinosphere, the neutrino diffusion process controls the magnitude of the diffusion coefficients, except the magnetic diffusivity (Thompson & Duncan 1993).

[6] The function $h(r, \theta, \phi)$ is an arbitrary function used only to explain three different averaging methods (volume, longitudinal, and spherical averages) adopted in our analysis and their notations in this paper. In the main body, h is replaced by the velocity v_i or the magnetic field B_i ($i=x, y, z$).

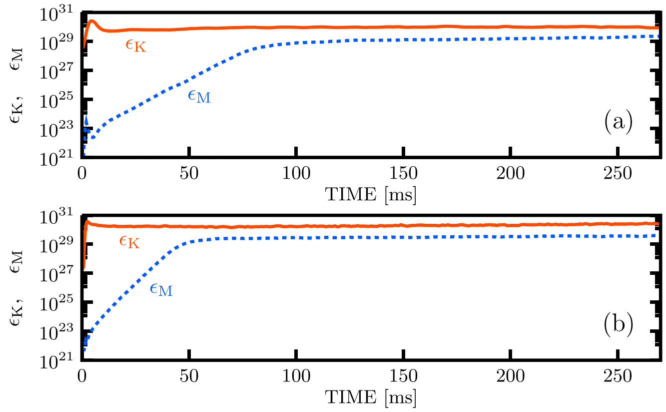

Figure 3. Temporal evolution of ϵ_K (red solid curve) and ϵ_M (blue dashed curve) for (a) model mf and (b) model ms.

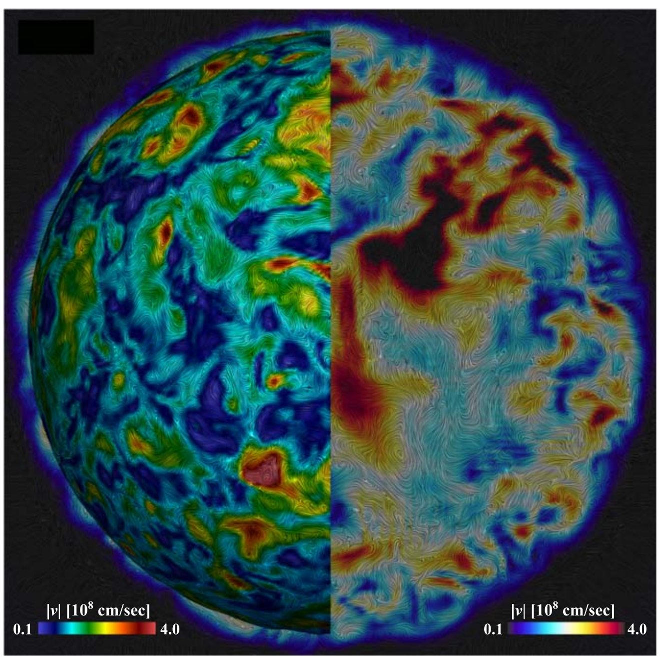

Figure 4. Line integral convolution (LIC) visualizations of $|\boldsymbol{v}|$ at $r = 15$ km (left hemisphere) and meridional cutting plane (right hemisphere) when $t = 230$ ms for model mf12p as a demonstration. The normalization unit is 10^8 cm s^{-1}. Red (blue) tone denotes higher (lower) convection velocity.

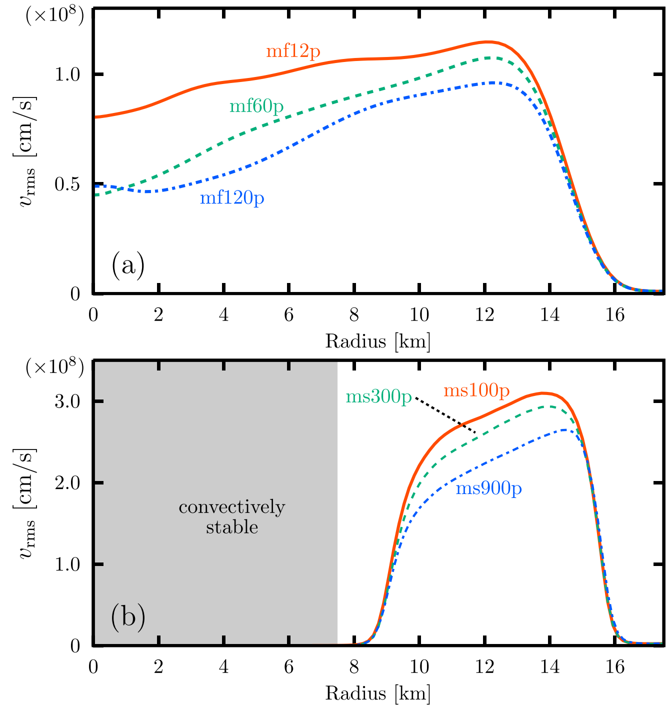

Figure 5. Radial profiles of $v_{\rm rms}$ for (a) models mf and (b) models ms at the equilibrated stage. The different line types correspond to models with different spin rates in each panel.

Browning 2017; Raynaud et al. 2020). See Table 1 for more details on the temporal means of ϵ_K and ϵ_M for each model.

The radial profiles of $v_{\rm rms}$ at the saturated stage for models (a) mf and (b) ms are shown in Figure 5, where $v_{\rm rms}$ is the rms of the perturbed radial velocity defined by $v_{\rm rms} \equiv \langle\langle(v_r - \langle\langle v_r\rangle_\phi\rangle)^2\rangle_s^{1/2}\rangle$. The different line types correspond to models with different spin rates. The shaded region in panel (b) denotes the convectively stable region.

Overall, the convection velocity is of the order of 10^8 cm s^{-1} although it is a few times higher in models ms than in models mf because of the larger thermal energy stored in model ms at the initial setup stage (see Figure 1). Since the rotational constraint, caused by the Coriolis force, on the convective motion becomes stronger in the model with the higher spin rate, the convection velocity decreases as the spin rate increases, which can be seen in each model (see Table 1).

As a corollary of the turbulent convective motion regulated by the rotation, large-scale flow and thermodynamic and magnetic structures are built up in the PNS. In the following, we will discuss in detail the results obtained with each model.

3.2. Models mf: Full-sphere Convection Models

3.2.1. Mean Flow and Thermodynamic Fields

Meridional distributions of (a) $\langle\langle v_\theta\rangle_\phi\rangle$, (b) $\delta\epsilon \equiv \langle\langle\epsilon - \langle\langle\epsilon\rangle_s\rangle\rangle_\phi\rangle$, and (c) $\Omega \equiv \langle\langle v_\phi\rangle_\phi\rangle/r\sin\theta + \Omega_0$ are shown in Figure 6. The overplotted arrows in panel (a) are meridional velocity vectors with arbitrary amplitudes. Panels (a1)–(c1) are for mf12p, (a2)–(c2) are for mf60p, and (a3)–(c3) are for mf120p.

From the symmetry point of view, the large-scale flows seen in models mf can be divided into two types: (i) a single-cell meridional circulation with a north–south antisymmetric differential rotation (mf12p), and (ii) a double-cell meridional circulation (one cell per hemisphere) with a cylindrical differential rotation (mf60p and mf120p). While the dipole dominance in $\delta\epsilon$ is accompanied by flow pattern (i), it can be seen that the quadrupolar dominance in $\delta\epsilon$ is developed in conjunction with pattern (ii).

The single-cell counterclockwise profile with circulation between northern and southern hemispheres, seen in Figure 6(a1), should be due to the very slow spin of mf12p. As shown in Chandrasekhar (1961) (see Section 59), the dipole dominance of the convective flow is a natural topological result of the full-sphere convection domain. See Section 3.3.1 for related discussion. Since the northern and southern hemispheres are dominated respectively by cool (and fast) downflow and warm (and slow) upflow, a large-scale coherent circulation is formed between them, resulting in the antisymmetric profile of $\delta\epsilon$ with respect to the equator

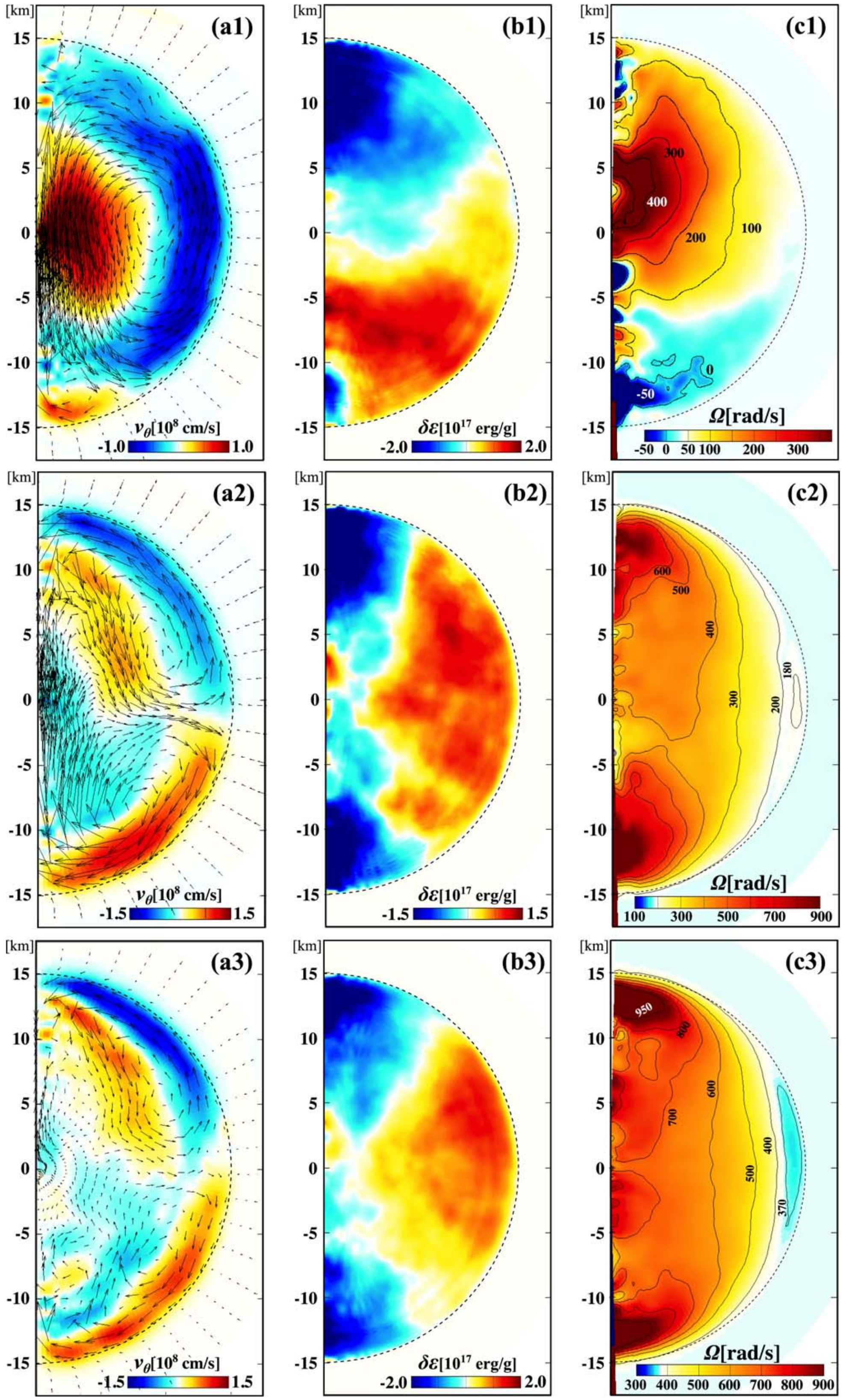

Figure 6. Meridional distributions of (a) $\langle\langle v_\theta\rangle_\phi\rangle$, (b) $\delta\epsilon$, and (c) Ω for model mf. The top, middle, and bottom panels correspond to models mf12p, mf60p, and mf120p, respectively. In panel (a), the streamlines are overplotted with arrows of length proportional to the flow velocity. In panel (c), the region rotating with the reference frame Ω_0 is shown in white. The isorotation contours are also overplotted.

(see Figure 6(b1)). The difference in $\delta\epsilon$ between hemispheres is 4×10^{17} erg g^{-1} on average, which provides 10^{50}–10^{51} erg when considering the total mass of the PNS.

The profile of Ω for mf12p (Figure 6(c1)) should be determined to retain a quasi-steady convective state: the production of vorticity by the baroclinic term ($\propto\partial\overline{\epsilon}/\partial\theta$)

should be balanced mainly by the production of relative vorticity by the stretching ($\propto \partial\Omega/\partial z$), that is, the thermal wind balance

$$\frac{\partial \omega}{\partial t} = r \sin\theta \frac{\partial \Omega^2}{\partial z} - \frac{g}{\gamma \bar{\bar{\epsilon}}} \frac{\partial \bar{\epsilon}}{\partial \theta} \cdots = 0 \tag{14}$$

should be maintained to retain the steady state, where ω is the vorticity and $\bar{\epsilon}$ is the time and azimuthally averaged specific internal energy. Note that this equation can be obtained as the meridional component of the mean-field equation of motion (see, e.g., Pedlosky 1982; Masada 2011).

Equation (14) predicts that the latitudinal variation of $\bar{\epsilon}$ produces a change in Ω in the z-direction. Since $\partial\bar{\epsilon}/\partial\theta \gtrsim 0$ over the entire CZ in mf12p, the spin rate should increase in the z-direction to satisfy Equation (14). This is qualitatively consistent with what we observe in mf12p, i.e., differential rotation with a north–south antisymmetry, which progrades in the northern hemisphere of the PNS and retrogrades in the southern one (see Figure 6(c1)). The overall mean properties of the hydrodynamics seen in mf12p are analogous to those in Brun & Palacios (2009) (see their model labeled RG2) though their simulated object is the red giant, which is different from ours.

The profile of the meridional flow seen in models mf60p and mf120p consists of a double-cell circulation (one cell per hemisphere, see Figure 6(a2) or (a3)). While it is poleward in the upper CZ, it reverses to an equatorward direction at greater depths. In such a case, the polar and equatorial regions are dominated respectively by cool downflow and warm upflow, naturally resulting in the quadrupolar structure of the thermodynamic field seen in the profile of $\delta\epsilon$ (Figure 6(b2) or (b3)). This type of circulation flow is often seen in convection simulations of slowly rotating solar-type stars with thin CZs (e.g., Mabuchi et al. 2015). The driving mechanism of such a double-cell circulation (one cell per hemisphere) will be discussed in detail in Section 3.3.1 because a similar profile can be observed even in models ms.

A remarkable property of the differential rotation achieved in mf60p and mf120p is that it is almost invariant along the rotation axis, i.e., $\partial\Omega/\partial z \simeq 0$ (see Figure 6(c2) or (c3)). It is well known that, according to the Taylor–Proudman constraint, the fluid parcel tends to move and thus its velocity tends to be uniform along the rotation axis in a system with sufficiently large Coriolis force (Pedlosky 1982; Kitchatinov & Ruediger 1995; Brun & Toomre 2002; Miesch et al. 2006; Masada 2011). The latitudinal variation of Ω is the antisolar type, that is the spin rate is lower at the equator than in the polar regions. Antisolar type differential rotation is also a characteristic feature of a relatively slowly spinning system. It should be noted that the overall mean flow properties in mf60p and mf120p are also analogous to those in Brun & Palacios (2009) (see their model labeled RG1), where the deep core convection in a red giant is discussed.

3.2.2. Magnetic Field: Dynamo Activities

The magnetic field, which is amplified by the PNS convection, shows a complicated structure mixed with the turbulent and large-scale components. Primarily, the turbulent convective motion produces small-scale intense magnetic fields. Figure 7 shows, as a demonstration, the distribution of the radial component of the magnetic field on spherical surfaces at different depths for mf12p in the Mollweide projection. A red (blue) tone denotes a positive (negative) value of the field strength. It is found that the turbulent component of the magnetic field becomes predominant inside the PNS. It is amplified via a small-scale convective dynamo (e.g., Cattaneo 1999; Schekochihin et al. 2004) and finally reaches a strength of $\mathcal{O}(10^{16})$ G, which contains about 30% of the convective kinetic energy at the saturated stage (see Figure 3 and Table 1). Turbulent magnetic components show similar characteristics in other full-sphere convection models, i.e., mf60p and mf120p.

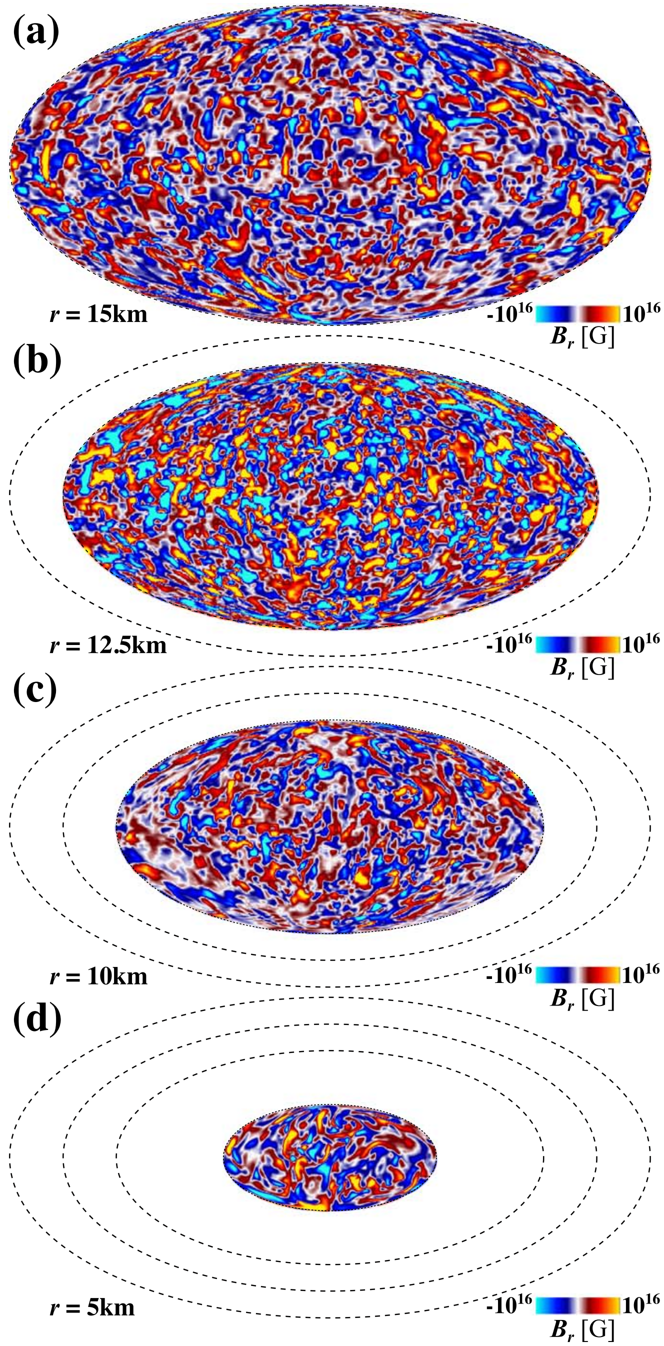

Figure 7. Distributions of the radial component of the magnetic field on spherical surfaces at sampled radii $r = 15$ km, 12.5 km, 10 km, and 5 km when $t = 230$ ms in the Mollweide projection for model mf (mf12p) as a reference.

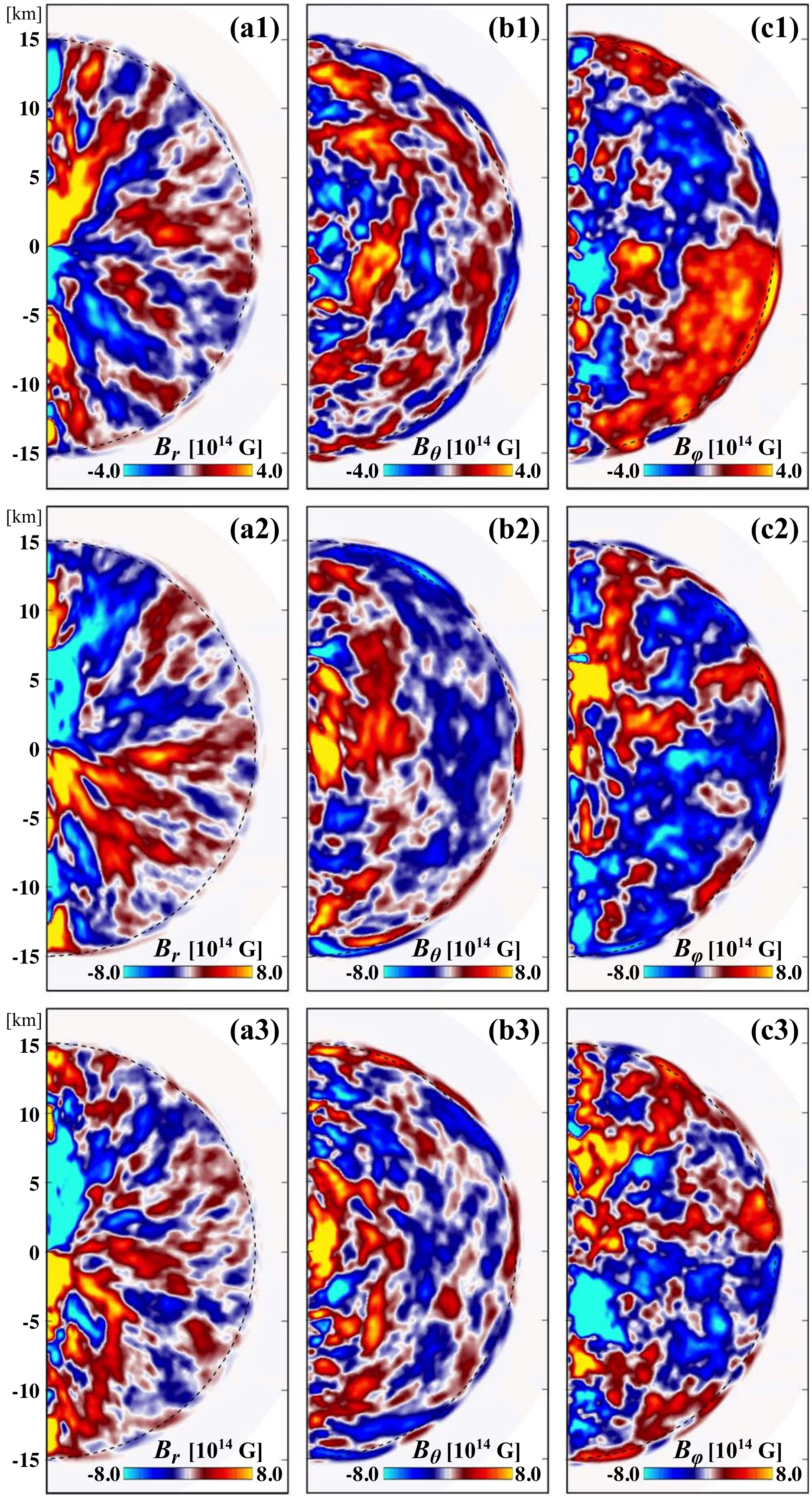

Figure 8. Meridional distributions of large-scale magnetic components: (a) $\langle\langle B_r\rangle_\phi\rangle$, (b) $\langle\langle B_\theta\rangle_\phi\rangle$, and (c) $\langle\langle B_\phi\rangle_\phi\rangle$ for model mf. The top, middle, and bottom panels correspond to models mf12p, mf60p, and mf120p, respectively. The time average is taken over durations 220 ms $\leqslant t \leqslant$ 240 ms.

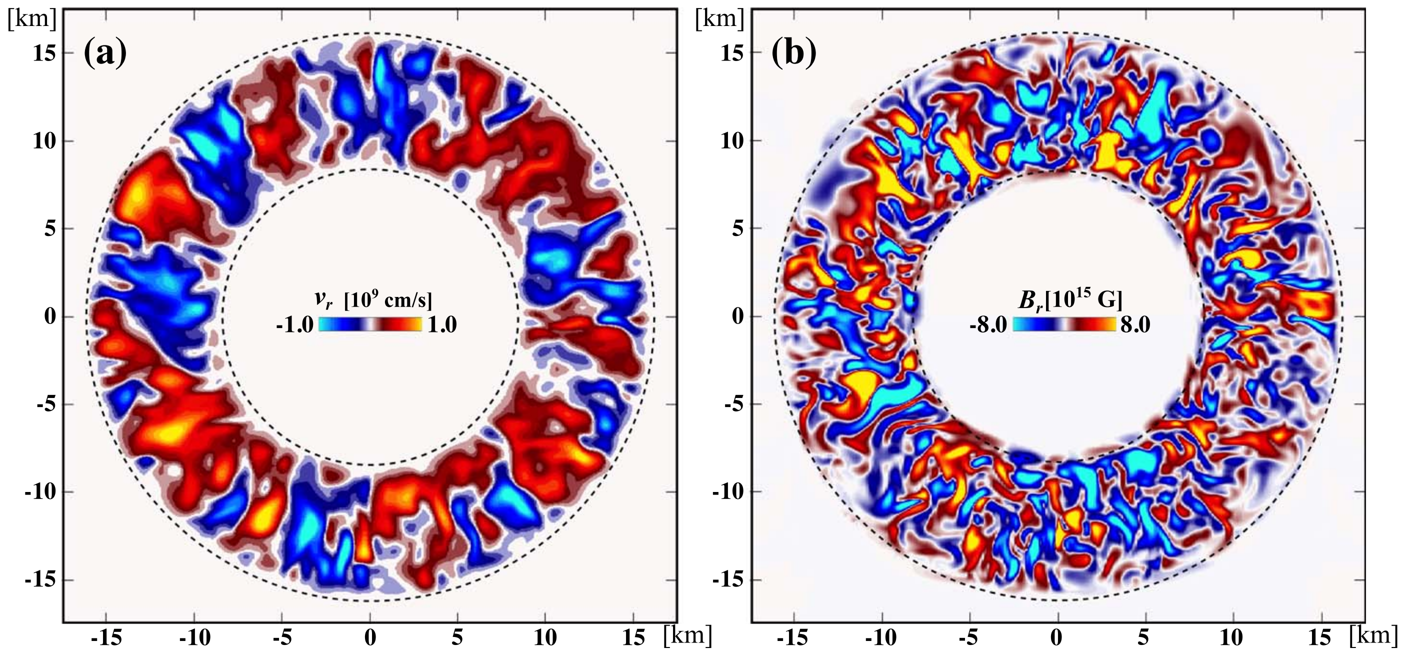

Figure 9. Instantaneous snapshots for the distributions of (a) v_r and B_r when $t = 220$ ms for model ms (ms100p) at the meridional cutting plane. A red (blue) tone denotes positive (negative) values.

In such a haystack of turbulent magnetic components, the large-scale magnetic structure is spontaneously organized in models mf. Shown in Figure 8 are the meridional distributions of large-scale magnetic components: (a) $\langle\langle B_r\rangle_\phi\rangle$, (b) $\langle\langle B_\theta\rangle_\phi\rangle$, and (c) $\langle\langle B_\phi\rangle_\phi\rangle$ for models mf. The top, middle, and bottom panels correspond to models mf12p, mf60p, and mf120p, respectively. The time average is taken over durations 220 ms $\leqslant t \leqslant$ 240 ms. A red (blue) tone denotes a positive (negative) magnetic field strength.

Commonly, the global structure of the mean magnetic component exhibits a dipole dominance in these models. It can be found that the large-scale poloidal component, rooted deep in the central part of the PNS, shows a strong dipole symmetry, while it is less coherent in the outer part of the sphere. Its strength reaches $\mathcal{O}(10^{14})$ G on average (and locally exceeds 10^{15} G), which is compatible with that expected in strongly magnetized NSs, so-called "magnetars" (e.g., Turolla et al. 2015; Enoto et al. 2019, and references therein). Additionally to the poloidal component, a large-scale toroidal magnetic component is also built up, mainly in the outer part of the PNS, especially in the relatively slowly spinning models (mf12p and mf60p). It is roughly antisymmetric with respect to the equator and also has an average strength of $\mathcal{O}(10^{14})$ G, which is a bit weaker than the poloidal component.

The large-scale magnetic component observed in *models* mf would be a self-organized structure as a natural outcome of the symmetry breaking forced by the NS's spin. Although a successful large-scale dynamo has been observed in a lot of solar, stellar, and planetary MHD convection simulations (e.g., Ghizaru et al. 2010; Käpylä et al. 2012; Masada et al. 2013; Fan & Fang 2014; Hotta et al. 2016) (see Charbonneau 2020 for a review), our intriguing finding here is that the large-scale field can be organized even in a rotation regime slower than that predicted by TD93. The dependence of the larges-scale magnetic field on the spin rate and the mechanism for the large-scale dynamo observed in our simulation models are discussed comprehensively in Section 4.

3.3. Models ms: Spherical-shell Convection Models

3.3.1. Mean Flow and Thermodynamic Fields

Unlike models mf with the full-sphere CZ, the turbulent convective motion is confined within the spherical-shell in models ms as presented in Figure 9(a), where an instantaneous snapshot for the profile of v_r on a meridional cutting plane for ms100p is shown. The convection velocity becomes maximum in the upper part of the CZ as shown in Figure 2(b), and locally reaches $\mathcal{O}(10^9)$ cm s^{-1}. The symmetry of the system is broken by the spinning motion of the PNS, resulting in an off-diagonal component of the Reynolds stress, which in turn gives rise to the mean flow and the large-scale thermodynamic structure even in models ms.[7]

Meridional distributions of (a) $\langle\langle v_\theta\rangle_\phi\rangle$, (b) $\delta\epsilon \equiv \langle\langle \epsilon - \langle\langle\epsilon\rangle_s\rangle\rangle_\phi\rangle$, and (c) $\Omega \equiv \langle\langle v_\phi\rangle_\phi\rangle / r\sin\theta + \Omega_0$ for models ms are shown in Figure 10. The overplotted arrows in panel (a) are meridional velocity vectors with arbitrary amplitudes. Panels (a1)–(c1) are for ms100p, (a2)–(c2) are for ms300p, and (a3)–(c3) are for ms900p.

From the symmetry point of view, the large-scale flows seen in models ms can be divided roughly into two types: (i) multicell meridional circulations with a shellular differential rotation (ms100p), and (ii) a double-cell meridional circulation (one cell per hemisphere) with a cylindrical differential rotation (ms300p and ms900p). In ms100p with the lowest spin rate, the

---

[7] When the large-scale magnetic field grows, magnetic braking may carry the angular momentum outside the CZ. However, as can be seen in Figure 6 or 10, there is no significant change in the angular velocity outside the CZ in our models. In our model, taking account of the existence of the convectively stable layer surrounding the CZ in the PNS, we put the damping region outside the CZ. We control the flow velocity there to be almost the same as in the initial state (i.e., $\boldsymbol{v} = 0$), resulting in the redistribution of the angular momentum only inside the CZ.

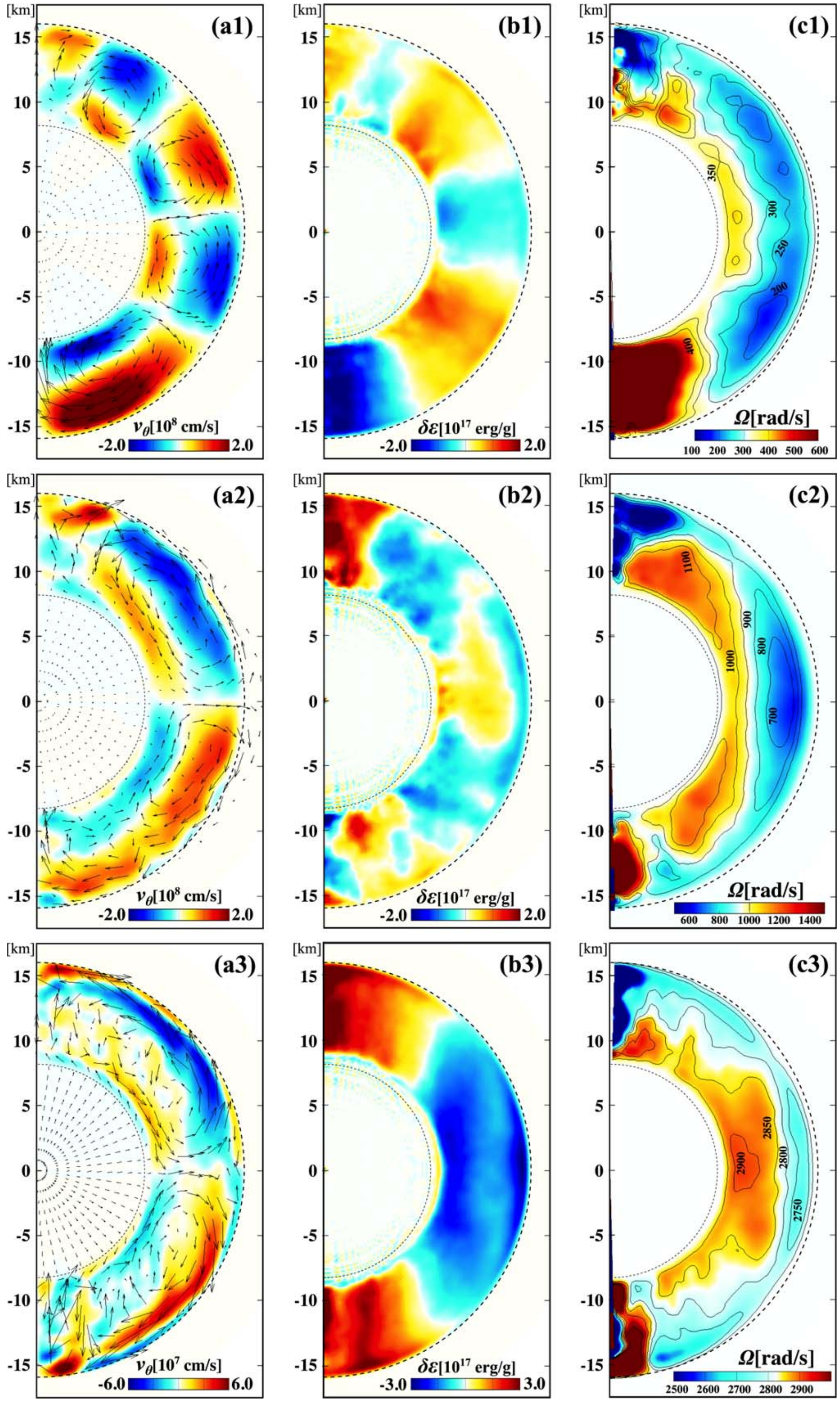

Figure 10. Meridional distributions of (a) $\langle\langle v_\theta\rangle_\phi\rangle$, (b) $\delta\epsilon \equiv \langle\langle\epsilon - \langle\langle\epsilon\rangle_s\rangle\rangle_\phi\rangle$, and (c) $\Omega \equiv \langle\langle v_\phi\rangle_\phi\rangle / r\sin\theta + \Omega_0$ for models ms. The top, middle, and bottom panels correspond to models ms100p, ms300p, and ms900p, respectively. In panel (a), the streamlines are overplotted with arrows of length proportional to the flow velocity. In panel (c), the region rotating with the reference frame Ω_0 is shown in white. The isorotation contours are also overplotted.

multipolar structure of the thermodynamic field is developed due to the multicell circulation flow. On the other hand, a quadrupolar structure of the thermodynamic field, which is similar to that in mf60p and mf120p (see Figures 6(b2) and (b3)), can be observed in the models with higher spin rates (ms300p and ms900p).

In the case of thin spherical-shell convection, like that operating in the Sun, it is well known that the multicell pattern of the meridional flow is often observed in the faster rotation regime: the transition from the single-cell (one per hemisphere) to multicell profiles of the circulation occurs when the spin rate increases (e.g., Featherstone & Miesch 2015; Mabuchi et al. 2015). However, intriguingly, our PNS models with spherical-shell convection appear to show the opposite behavior: a single-cell (one per hemisphere) pattern appeared in faster rotating models (ms300p and ms900p), and the multicell pattern in a slowly rotating model (ms100p).

The single-cell (one per hemisphere) circulation can be qualitatively understood by so-called "gyroscopic pumping": when assuming the quasi-steady state, the equation for the conservation of angular momentum can be derived from the zonal component of the mean-field equation of motion as

$$\overline{\rho \boldsymbol{v}_{\rm M}} \cdot \nabla \mathcal{L} = -\nabla \cdot \boldsymbol{\mathcal{F}}_{\rm RS}, \quad (15)$$

where the overbar denotes the time and longitudinal average, $\boldsymbol{v}_{\rm M}$ is the velocity of the meridional flow component, $\mathcal{L} \equiv \varpi^2\Omega = \varpi\langle\langle v_\phi\rangle_\phi\rangle + \varpi^2\Omega_0$ is the specific angular momentum ($\varpi = r\sin\theta$ is the cylindrical radius), and $\boldsymbol{\mathcal{F}}_{\rm RS}$ is the turbulent angular momentum flux by the convective Reynolds stress, which is described as

$$\boldsymbol{\mathcal{F}}_{\rm RS} \equiv \bar{\rho}\varpi(\overline{u_r{'}u_\phi{'}}\boldsymbol{e}_r + \overline{u_\theta{'}u_\phi{'}}\boldsymbol{e}_\theta). \quad (16)$$

Note that the other non-axisymmetric components of the stress, such as the Maxwell stress and molecular viscosity, are ignored because they are negligible in comparison to the Reynolds stress here.

Since the radial convection velocity is expected to be higher than the latitudinal and longitudinal velocities in a regime of relatively slow rotation, the angular momentum is transported mainly in the radially inward direction, that is $\boldsymbol{\mathcal{F}}_{\rm RS} \propto \overline{u_r{'}u_\phi{'}}\boldsymbol{e}_r$ with $\overline{u_r{'}u_\phi{'}} < 0$. Then, the right-hand side of Equation (15) becomes positive (negative) in the upper (lower) CZ because $\partial\mathcal{F}_{\rm RS}/\partial r > 0$ ($\partial\mathcal{F}_{\rm RS}/\partial r < 0$) in the upper (lower) CZ when $\mathcal{F}_{\rm RS} = 0$ at the top and bottom boundaries (e.g., Miesch 2005; Miesch & Toomre 2009; Schrijver & Siscoe 2010).

On the other hand, $\mathcal{L}$ (specific angular momentum) has a cylindrical profile and decreases monotonically from equator to pole, that is $\partial\mathcal{L}/\partial\theta < 0$ as shown in Figure 11, where the meridional distribution of the $\mathcal{L}$ in the northern hemisphere of ms900p is demonstrated. Note that a similar profile of $\mathcal{L}$ can be seen in ms300p. To retain the zonal momentum balance described by Equation (15), the meridional flow should be poleward (i.e., $\bar{v}_\theta < 0$) in the upper CZ while it should be equatorward (i.e., $\bar{v}_\theta > 0$) in the lower CZ, providing the single-cell (one per hemisphere) circulation flow seen in ms300p and ms900p. Note that the meridional flow observed in mf60p and mf120p should be driven by the same mechanism, that is the gyroscopic pumping.

The multicell pattern seen in ms100p (see Figure 10(a1)) might be a consequence of the convective motion characterized by thick CZ, slow spin, and relatively low Reynolds number.

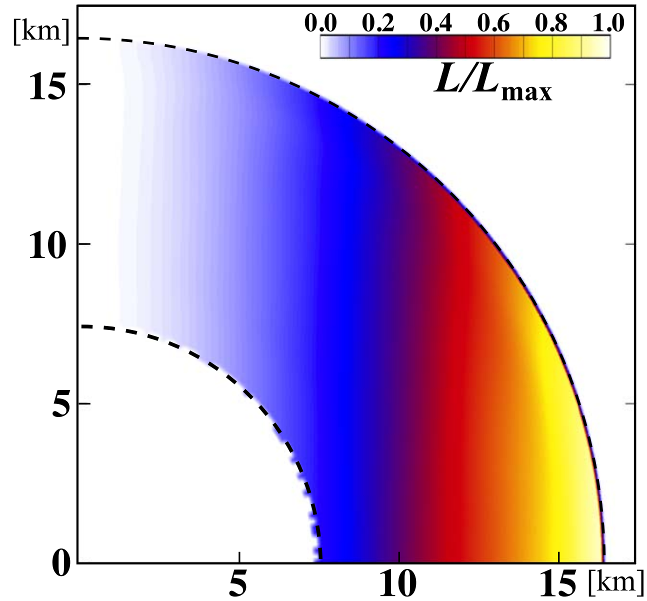

Figure 11. Meridional distribution of the normalized angular momentum, $\mathcal{L} \equiv \varpi^2\Omega$, in the northern hemisphere for models ms (ms900p). The normalization unit is the maximum value of $\mathcal{L}$, which corresponds to that on the equatorial surface.

According to Chandrasekhar (1961) (Section 59), the spherical harmonic degree of the most unstable mode for the convective instability depends on the thickness of the CZ and becomes lower as it increases. The higher the spherical harmonic degree of the mode, the lower the growth rate becomes. At the limit of no rotation, the mode with $l = 3$–4 seems to become the most unstable when the upper 40%–60% of the sphere is convective. In the system with small Reynolds and Rayleigh numbers, such as those expected in a PNS, the growth of the mode with larger spherical harmonic degree (i.e., $l \gtrsim 3$–4) and thus shorter wavelength tends to be suppressed. As a result, the pattern of the linear unstable mode with lower spherical harmonic degree might be imprinted in the mean flow field like the circulation flow seen in ms100p.

The profile of the differential rotation in ms300p and ms900p is cylindrical (Figures 10(c2) and (c3)), that is in the Taylor–Proudman state like mf60p and mf120p, the flow being nearly two-dimensional in the plane orthogonal to the spin axis (e.g., Pedlosky 1982; Kitchatinov & Ruediger 1995). The lower the spin rate is, the weaker the rotational constraint on the flow becomes, resulting in the shellular rotation profile seen in ms100p (Figure 10(c1)). Such a shellular rotation profile is also observed in Brun & Palacios (2009) for a slowly rotating red giant. As was described, the angular momentum transport in relatively slowly rotating systems is mainly in the radially inward direction, that is $\boldsymbol{\mathcal{F}}_{\rm RS} \propto \overline{u_r{'}u_\phi{'}}\boldsymbol{e}_r$ with $\overline{u_r{'}u_\phi{'}} < 0$. The faster spinning motion in the deeper CZ is thus a natural result of the turbulent transport process.

3.3.2. Magnetic Field: Dynamo Activities

As shown in Figure 9(b), the spherical-shell convective motion amplifies turbulent magnetic fields of $\mathcal{O}(10^{16})$ G via a small-scale dynamo process (e.g., Cattaneo 1999; Schekochihin et al. 2004). The magnetic energy contained in the turbulent magnetic component is larger at greater depths. When taking a time and zonal average, we can find, even in

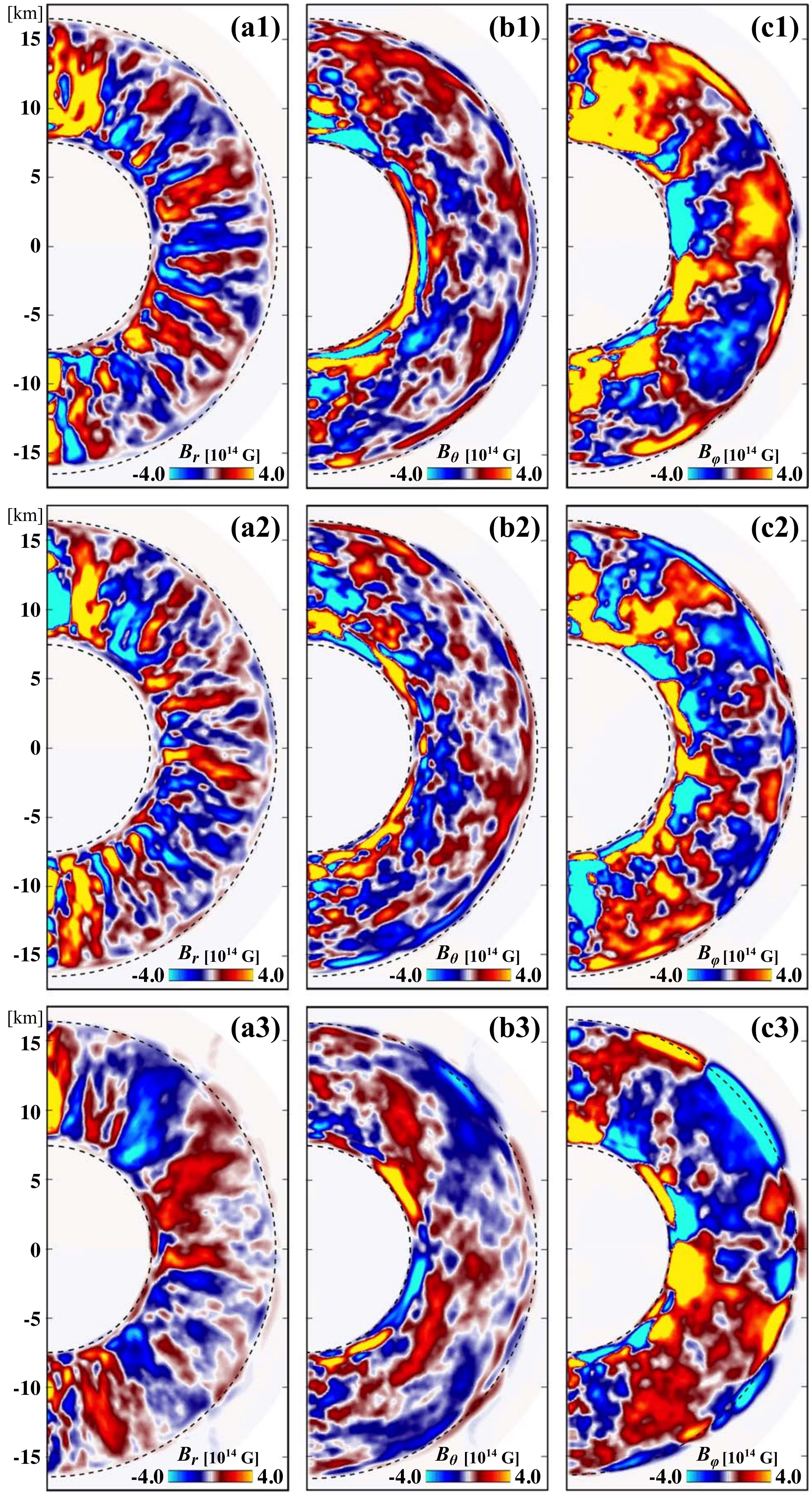

Figure 12. Meridional distributions of large-scale magnetic components: (a) $\langle\langle B_r\rangle_\phi\rangle$, (b) $\langle\langle B_\theta\rangle_\phi\rangle$, and (c) $\langle\langle B_\phi\rangle_\phi\rangle$ for model ms. The top, middle, and bottom panels correspond to models ms100p, ms300p, and ms900p, respectively. The time average is taken over durations 220 ms $\leqslant t \leqslant$ 240 ms.

models ms, that the large-scale component of the magnetic field is developed in these highly disordered magnetic fields.

In Figure 12, the meridional distributions of (a) $\langle\langle B_r\rangle_\phi\rangle$, (b) $\langle\langle B_\theta\rangle_\phi\rangle$, and (c) $\langle\langle B_\phi\rangle_\phi\rangle$ for models ms are shown. The top, middle, and bottom panels are for models ms100p, ms300p, and ms900p, respectively. The time average is taken over durations 220 ms $\leqslant t \leqslant$ 240 ms. A red (blue) tone denotes a positive (negative) magnetic field strength.

As in models mf, the mean component of the magnetic field has a strength $\mathcal{O}(10^{14})$ G on average and locally exceeds 10^{15} G, which is comparable to the field strength expected in "magnetars". When focusing on the geometry of the poloidal component of the magnetic field (B_r and B_θ), we can find it is more complicated than that observed in the models with the full-sphere convection: while the higher multipole structure becomes dominant in the models in the regime of relatively slow rotation (ms100p and ms300p), quadrupolar dominance is prominent in the fastest spinning model (ms900p). Additionally to the poloidal component, a large-scale toroidal magnetic component is also built up in all models. Commonly, it is roughly antisymmetric with respect to the equator and seems to be a bit "stronger" than the poloidal magnetic component. The dependence of the large-scale magnetic field on the spin rate and the mechanism for the large-scale dynamo observed in our simulation models are discussed in detail in the following section.

4. Discussion

4.1. Rotational Dependence of Large-scale Magnetic Field

As presented in Figures 8 and 12, the mean component of the magnetic field is spontaneously organized in all the PNS models we examined in this paper. Here we discuss the dependence of the structure and strength of the mean magnetic component on the spin rate of the PNS systematically.

To gain quantitative insights into it, the latitudinal moment of the axisymmetric field, $\bar{\boldsymbol{B}}$, is analyzed, where the overbar, used to simplify the notation, denotes the time and longitudinal average, i.e., $\bar{B}_r = \langle\langle B_r\rangle_\phi\rangle$. We focus on the radial component $\bar{B}_r$ since it purely reflects the poloidal field, while $\bar{B}_\theta$ and $\bar{B}_\phi$ are a mixture of the toroidal and poloidal fields. From Perseval's equation, a relation

$$\langle \bar{B}_r^2\rangle_\theta = \frac{1}{2}\sum_{l=1}(\bar{B}_r)_l^2, \tag{17}$$

where

$$(\bar{B}_r)_l = \int_{-1}^{1} \bar{B}_r P_l^*(\cos\theta) d\cos\theta, \tag{18}$$

holds (see Masada et al. 2013, for details). Here P_l^* are normalized Legendre polynomials. In the following, we focus on three larger-scale modes $l = 1$, 2, and 3 (dipole, quadrupole, and octupole) as an indicator of the efficiency of the large-scale dynamo.

Shown in Figure 13 is the radial distribution of the ratio of the magnetic energy stored in the largest-scale components ($l = 1$–3) to the total magnetic energy of the axisymmetric field, that is $\sum_{l=1}^{3}(\bar{B}_r)_l/2\langle\bar{B}_r^2\rangle_\theta$ for (a) models mf and (b) models ms. The different line types denote models with different spin rates. The gray shaded region in panel (b) corresponds to the convectively stable region of models ms.

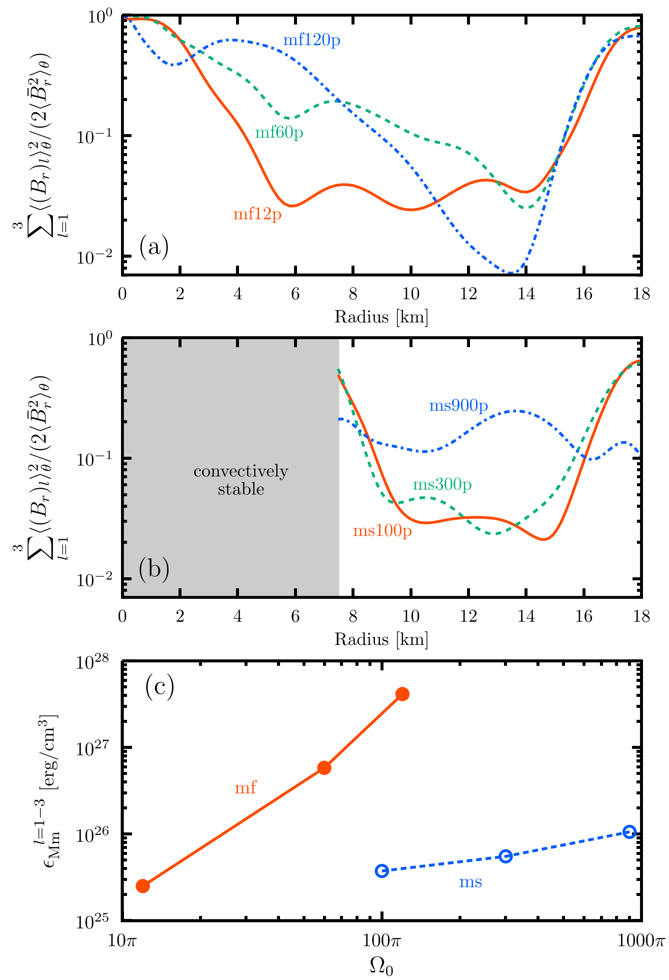

Figure 13. Radial distributions of the dominance of the large-scale field for (a) models mf and (b) models ms. The different line types denote models with different spin rates. Panel (c) shows the dependence of the mean magnetic energy of the large-scale magnetic field on the spin rate for model mf (red solid curve) and model ms (blue dashed curve).

Note that the higher the ratio, the more the large-scale field becomes dominant.

For models mf (panel (a)), the dominance of the large-scale component in the magnetic energy is more pronounced in the deeper CZ and decreases with the radius, suggesting that the dynamo effect is stronger at greater depth. Interestingly, even in mf12p with the smallest spin rate (red solid line), the central part of the PNS ($r \lesssim 5$ km) is occupied by the large-scale component, which is consistent with the result of Figure 8. As the spin rate increases, the region where the large-scale magnetic component becomes dominant extends into the outer part of the CZ, implying that the dynamo effect becomes stronger for a higher spin rate of the PNS.

Comparing models mf and ms, the dominance of the large-scale magnetic component seems to be weaker in the models ms. It is a common feature of all the models that the strong large-scale component is developed near the upper and lower boundaries, but in the middle part of the CZ, only model ms900p shows a strong large-scale magnetic component (blue dashed–dotted line in panel (b)). This implies that the large-scale dynamo can be excited in the middle part of the CZ only when the PNS's spin is fast enough.

Figure 13(c) shows the dependence on the spin rate of the mean magnetic energy stored in the large-scale component defined by

$$\epsilon_{\mathrm{Mm},l=1-3} = \sum_{l=1}^{3}\left[\int_{r_{\min}}^{r_{\max}} (\bar{B}_r)_l^2 dr \Big/ \int_{r_{\min}}^{r_{\max}} dr\right], \quad (19)$$

where $r_{\min}$ and $r_{\max}$ are the pseudo-upper and -lower boundaries of the CZ. We choose $r_{\min} = 0$ km and $r_{\max} = 17$ km for models mf and $r_{\min} = 7.5$ km and $r_{\max} = 17.5$ km for models ms.

Commonly in both models, we can find a clear tendency for the mean magnetic energy stored in the large-scale component to increase with the spin rate. However, there exists a difference in the strength of the dependence on the spin rate. In the regime we studied in this paper, the slope of the spin dependence is steeper in models mf than in models ms. It would be necessary to investigate the dependence of the PNS dynamo on the spin rate in a wider parameter range to understand the difference in the trends.

4.2. Dynamo Mechanism

It is well known that the rotating convection system spontaneously generates a mean kinetic helicity with a north–south antisymmetry, i.e., in the case of eastward spinning motion like our PNS model, bulk negative helicity in the north and positive in the south, because of the Coriolis force acting on the convection flow (e.g., Miesch 2005; Miesch & Toomre 2009). From preceding studies on stellar and solar dynamos (e.g., Charbonneau 2014, 2020; Brun & Browning 2017, for reviews), we expect that the turbulent electromotive fore (EMF) would be the key for generating the large-scale magnetic component even in our PNS models (e.g., Racine et al. 2011; Masada & Sano 2014).

Although it is difficult to evaluate quantitatively the role of the turbulent EMF in the complicated PNS models, we can appraise it at least qualitatively based on the mean-field dynamo (MFD) theory. Under the first-order smoothing approximation (e.g., Brandenburg & Subramanian 2005; Masada & Sano 2014), the kinetic helicity would be closely linked to the turbulent α-effect, which is a key ingredient of most MFD models (e.g., Moffatt 1978; Krause & Raedler 1980), by

$$\alpha \equiv -\tau_{\mathrm{cor}}\langle\langle \boldsymbol{v}' \cdot \omega'\rangle_\phi\rangle/3, \quad (20)$$

where $\boldsymbol{v}' \equiv \boldsymbol{v} - \langle\langle \boldsymbol{v}\rangle_\phi\rangle$ is the turbulent velocity, τ_{cor} is the correlation time, and $\boldsymbol{\omega}' \equiv \nabla \times \boldsymbol{v}'$ is the turbulent vorticity. In addition to this, the turbulent magnetic diffusivity, which parameterizes the turbulent transport of the magnetic energy through advection and reconnection and thus controls the destruction of the large-scale magnetic field, is linked to the turbulent velocity as

$$\eta_t \equiv \tau_{\mathrm{cor}}\langle\langle \boldsymbol{v}'^2\rangle_\phi\rangle/3. \quad (21)$$

Essentially, these parameterizations for α and η_t are valid only in isotropic turbulence (e.g., Schrijver & Siscoe 2010). However, even in anisotropic turbulence, they have been shown to be useful in studying the ability of a system to excite the large-scale dynamo (e.g., Racine et al. 2011; Masada & Sano 2014).

In Equations (20) and (21), the correlation time can be evaluated as the convective turnover time, that is $\tau_{\mathrm{cor}} = H_\rho/\langle v_r^2\rangle^{1/2}$, where H_ρ is the density scale height. Since $\boldsymbol{v}'$, $\boldsymbol{\omega}'$, and H_ρ can be extracted from the simulation data directly, we can depict meridional distributions of the turbulent α and turbulent magnetic diffusivity for each model. In the following, we discuss the hidden connection between the large-scale magnetic component observed in our PNS models and the turbulent EMF by using a dimensionless parameter $\mathcal{C}_\alpha$ defined by

$$\mathcal{C}_\alpha = \alpha H_\rho/\eta_t, \quad (22)$$

which is equivalent to the so-called "dynamo number" when H_ρ is chosen as a typical spatial scale on which the large-scale dynamo works. Since α and η_t describes the induction and destruction effects of the large-scale magnetic component respectively, the amplitude of $\mathcal{C}_\alpha$ becomes a measure of the efficiency of the large-scale dynamo.

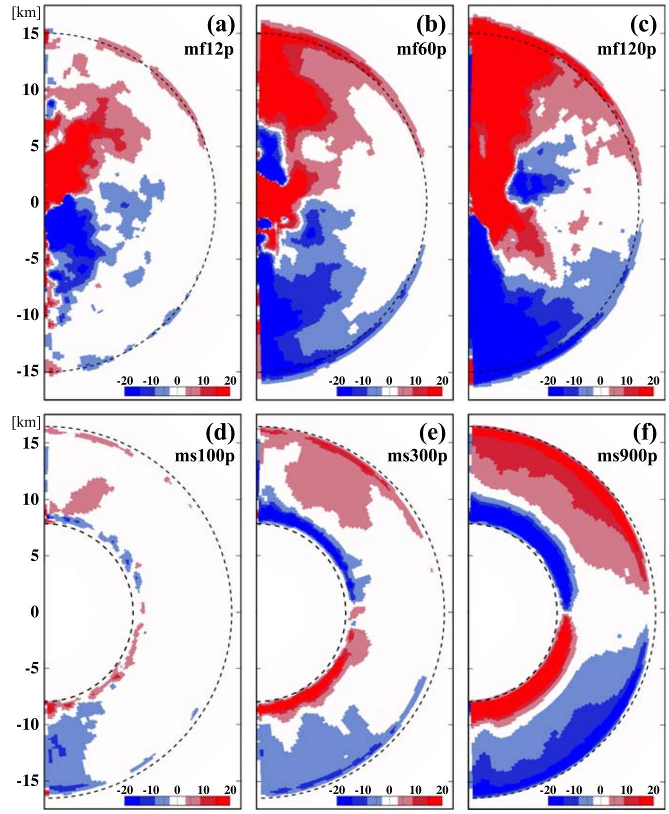

Figure 14. Meridional distributions of $\mathcal{C}_\alpha = \alpha H_\rho/\eta_t$ for (a)–(c) models mf and (d)–(f) models ms.

Shown in Figure 14 is the meridional distribution of $\mathcal{C}_\alpha$, which is derived directly from the simulation data obtained in each model. Panels (a)–(c) correspond to those in models mf and panels (d)–(f) are for models ms. Note that the color scale is the same for all panels. The darker the color, the stronger the relative induction effect becomes.

Since the kinetic helicity has an antisymmetric profile with respect to the equator (bulk negative in the north and positive in the south), the profile of $\mathcal{C}_\alpha$ also shows the quasi-antisymmetry between hemispheres. With comparing Figures 13 and 14, it can be found that there exists a remarkable overlap between the region with the strong large-scale magnetic component and the region with the large $|\mathcal{C}_\alpha|$ in both models. In addition, the region with the large $|\mathcal{C}_\alpha|$ extends into the outer part of the CZ like that observed in the large-scale magnetic component. Comparing two models, we can see that the amplitude of C_α is larger in models mf than in models ms, suggesting higher efficiency of the large-scale dynamo in models mf. This is consistent with the stronger large-scale magnetic component in models mf seen in Figure 13(c). Overall these results suggest that the turbulent EMF plays an important role in the large-scale dynamo in our PNS models.

Then, a natural question arises: "Why is the efficiency of the large-scale dynamo higher in models mf though the spin rate of models mf is smaller than that of models ms?" The key would be the typical size and velocity of the convective motion. The turbulent α-effect can be expressed in the form

$$\alpha = -\frac{1}{3}\tau_{\rm cor}^2 \boldsymbol{v}'^2[\boldsymbol{\Omega}\cdot\nabla\ln(\overline{\rho \boldsymbol{v}'})], \tag{23}$$

(e.g., Steenbeck & Krause 1969; Charbonneau 2013) if we assume that the inhomogeneity arises from the stratification and the symmetry breaking from the Coriolis force, and the lifetime of turbulent eddies is evaluated as the their turnover time. With this description, the dynamo number $\mathcal{C}_\alpha$ can be rewritten as

$$\begin{aligned}\mathcal{C}_\alpha &= \alpha H_\rho/\eta_t \\ &\simeq \Omega H_\rho \cos\theta/v_{\rm rms} \propto Ro^{-1},\end{aligned} \tag{24}$$

with a rough estimation $\nabla\ln(\overline{\rho \boldsymbol{v}'}) \simeq 1/H_\rho$. When ignoring the latitudinal dependence, we can see that the dynamo number, which is a measure of the efficiency of the large-scale dynamo, is a function of the spin rate, the scale height, and the velocity of the turbulent convective motion.

On the whole, models mf are assumed to have lower spin rates than models ms. On the other hand, as shown in Figures 2 and 5, models mf haves a lower convection velocity and a larger size of the convective eddies, especially in the central part of the PNS. These results indicate that the larger $\mathcal{C}_\alpha$ realized in models mf is a consequence of the smaller convection velocity and larger size of the convective eddies (especially in the deeper CZ), which compensate for its smaller spin rate, resulting in an environment more suitable for the large-scale dynamo. It can be said that, physically, the deeper the CZ extends, the larger the size of the convective eddies, and thus rotationally constrained convection is more easily achieved, resulting in a region more suitable for the large-scale dynamo.

5. Summary

In this paper, we constructed a "PNS in a box" simulation model by solving the compressible MHD with a nuclear EOS and simplified leptonic transport to study the properties of MHD convection and the dynamo in PNSs. As a demonstration of our newly developed model, we applied it to two types of internal structure of the PNS: a fully convective state and a spherical-shell convection state. Our main findings are summarized as follows.

1. The large-scale flows developed in models mf are divided into two types: (i) a single-cell meridional circulation with a north–south antisymmetric differential rotation (mf12p), and (ii) a double-cell meridional circulation (one cell per hemisphere) with a cylindrical differential rotation (mf60p and mf120p). While the dipole dominance in $\delta\epsilon$ is accompanied by flow pattern (i), the quadrupolar dominance in $\delta\epsilon$ is developed in conjunction with pattern (ii).
2. The large-scale flows developed in models ms are also divided into two types: (i) multicell meridional circulations with a shellular differential rotation (ms100p), and (ii) a double-cell meridional circulation (one cell per hemisphere) with a cylindrical differential rotation (ms300p and ms900p). While the multipolar structure of $\delta\epsilon$ is accompanied by flow pattern (i), the quadrupolar structure of $\delta\epsilon$ is developed in models with higher spin rates.
3. Taking account of the angular momentum transport due to the turbulent Reynolds stress caused by rotating convective motions, the circulation pattern of the formed meridional flow can be qualitatively understood by so-called "gyroscopic pumping". On the other hand, the profile of the differential rotation is determined to maintain the thermal wind balance of the system.
4. The magnetic field amplified by the PNS convection shows a complicated structure mixed with the turbulent and large-scale components. It should be emphasized that, in all the PNS models we studied here, the large-scale component of the magnetic field is spontaneously organized. For models mf, the mean magnetic component exhibits a dipole dominance, i.e., the large-scale poloidal component, rooted deep in the central part of the PNS, shows a strong dipole symmetry. In contrast, for models ms, while the higher multipole structure becomes dominant in models in a regime of relatively slow rotation, quadrupolar dominance is prominent in the fastest spinning model.
5. Although there exists a clear tendency for the mean magnetic energy stored in the large-scale component to increase with the spin rate in both models, the slope of the spin dependence is steeper in models mf than in models ms. Additionally, it is intriguing that, as an overall trend, models mf have a stronger large-scale magnetic component than models ms.
6. There exists a remarkable overlap between the region with a strong large-scale magnetic component and the region with large $|\mathcal{C}_\alpha|$ in both models, where $\mathcal{C}_\alpha$ is equivalent to the so-called "dynamo number" and a measure of the efficiency of the large-scale dynamo. Comparing two models, the amplitude of $\mathcal{C}_\alpha$ is larger in models mf than in models ms, suggesting a higher efficiency of the large-scale dynamo in models mf. Since the deeper the CZ extends, the larger the size of the convective eddies, rotationally constrained convection seems to be more easily achieved in models mf. As a result, the full-sphere convection state becomes more suitable for the large-scale dynamo.

Although the convective dynamo is believed conventionally to work only in rapidly rotating PNSs (e.g., TD93), a clear dynamo activity can be found even in a slowly rotating PNS with $P_{\rm rot} \simeq 170$ ms (mf12p). This would be essentially due to the setup of models mf in which the CZ extends to the deeper part of the PNS. It is well known that the width of the CZ in the PNS changes depending not only on the physical properties of the progenitor star (e.g., Nagakura et al. 2020) but also on the evolutionary phase of the PNS. As demonstrated in the 2D hydrodynamic simulation of the deleptonization of the PNS by Keil et al. (1996), the CZ in the PNS enlarges to the deeper part with the progress of neutrino cooling, finally encompassing the whole star within ~1 s after bounce, and can continue for at least as long as deleptonization takes place (see also Roberts et al. 2012).

Since most of the existing studies of the PNS dynamo suppose the early evolutionary stage at which only the outer part of the PNS is convective, the scale height, and thus the size of the convective eddies, is relatively small there, resulting in high $\mathcal{C}_\alpha$ in a case with slow or moderate rotation (e.g., TD93). On the other hand, at a later evolutionary stage, the PNS is expected to have a deeper CZ with a larger size of the convective eddies in the deeper part, like the fully convective models we studied here. In such a situation, the Coriolis force dominates over the inertia force around the PNS core, and thus the large-scale magnetic component might be efficiently amplified there by the turbulent α-effect against the turbulent magnetic diffusion, i.e., the region with $\mathcal{C}_\alpha \gg 1$ might be more easily developed. Overall our results imply that the PNS dynamo may become more efficient in later phases of its evolution. We note that the importance of deep core convection for the large-scale dynamo has already been pointed out in the study of the origin of the magnetic field in fully convective M-type dwarfs (Yadav et al. 2016; Käpylä 2021).

Recently, Beniamini et al. (2019) studied the formation rate of Galactic magnetars directly from observations and estimated that a fraction of $0.4^{+0.6}_{-0.28}$ of NSs are born as magnetars with magnetic fields of $B \gtrsim 3 \times 10^{13}$ G. This finding is a challenge to standard scenarios for magnetar formation, because these scenarios require more or less extreme conditions, such as pre-collapse rapid rotation and/or strong magnetic fields. As a physical mechanism to explain a possibly high fraction of the magnetars in NSs, Soker (2020) proposed the stochastic omega effect and claimed that rapid rotation is not necessarily required for magnetar formation. Our studies in this paper also suggest that the strong magnetic fields expected in magnetars can be organized in newly born NSs even at relatively slow rotations, which may prompt a reconsideration of the existing scenarios for magnetar formation.

To build up a concrete view on the role of PNS convection in the context of the origin of an NS's magnetic fields, we should study MHD convection in a PNS in a wider parameter range, varying the depth of the CZ, diffusivities, the rotation rate, and the initial strength of the magnetic field. These are beyond the scope of this paper, but will be a target of our future work.

We acknowledge the anonymous referee for constructive comments. This work has been supported by MEXT/JSPS KAKENHI grant Nos. JP17H01130, JP17K14306, JP18H01212, JP18K03700, JP17H06357, JP17H06364, JP18H04444, JP21K03612; the Central Research Institute of Stellar Explosive Phenomena (REISEP) at Fukuoka University and the associated projects (grant Nos. 171042, 177103) and JICFuS as a priority issue to be tackled by using Post "K" Computer. Numerical computations were carried out on Cray XC50 at Center for Computational Astrophysics, National Astronomical Observatory of Japan.

ORCID iDs

Youhei Masada https://orcid.org/0000-0002-0767-3449
Tomoya Takiwaki https://orcid.org/0000-0003-0304-9283
Kei Kotake https://orcid.org/0000-0003-2456-6183

References

Beniamini, P., Hotokezaka, K., van der Horst, A., et al. 2019, MNRAS, 487, 1426
Bonanno, A., Rezzolla, L., & Urpin, V. 2003, A&A, 410, L33
Bonanno, A., Urpin, V., & Belvedere, G. 2006, A&A, 451, 1049
Brandenburg, A., & Subramanian, K. 2005, PhR, 417, 1
Brun, A. S., & Browning, M. K. 2017, LRSP, 14, 4
Brun, A. S., & Palacios, A. 2009, ApJ, 702, 1078
Brun, A. S., & Toomre, J. 2002, ApJ, 570, 865
Burrows, A., & Lattimer, J. M. 1988, PhR, 163, 51
Camelio, G., Dietrich, T., Marques, M., et al. 2019, PhRvD, 100, 123001
Cattaneo, F. 1999, ApJL, 515, L39
Chandrasekhar, S. 1961, Hydrodynamic and Hydromagnetic Stability (Oxford: Clarendon)
Charbonneau, P. 2013, Solar and Stellar Dynamos: Saas-Fee Advanced Course 39 (Berlin: Springer), 39
Charbonneau, P. 2014, ARA&A, 52, 251
Charbonneau, P. 2020, LRSP, 17, 4
Dobler, W., Stix, M., & Brandenburg, A. 2006, ApJ, 638, 336
Enoto, T., Kisaka, S., & Shibata, S. 2019, RPPh, 82, 106901
Epstein, R. I. 1979, MNRAS, 188, 305
Fan, Y., & Fang, F. 2014, ApJ, 789, 35
Featherstone, N. A., & Miesch, M. S. 2015, ApJ, 804, 67
Ferrario, L., Melatos, A., & Zrake, J. 2015, SSRv, 191, 77
Freytag, B., Steffen, M., & Dorch, B. 2002, AN, 323, 213
Ghizaru, M., Charbonneau, P., & Smolarkiewicz, P. K. 2010, ApJL, 715, L133
Hotta, H., Rempel, M., & Yokoyama, T. 2016, Sci, 351, 1427
Jones, C. A. 2011, AnRFM, 43, 583
Käpylä, P. J. 2021, A&A, 651, A66
Käpylä, P. J., Mantere, M. J., & Brandenburg, A. 2012, ApJL, 755, L22
Keil, W., Janka, H.-T., & Mueller, E. 1996, ApJL, 473, L111
Kippenhahn, R., & Weigert, A. 1990, Stellar Structure and Evolution (New York: Springer-Verlag)
Kitchatinov, L. L., & Ruediger, G. 1995, A&A, 299, 446
Krause, F., & Raedler, K.-H. 1980, Mean-field Magnetohydrodynamics and Dynamo Theory (Oxford: Pergamon)
Lattimer, J. M., & Swesty, D. F. 1991, NuPhA, 535, 331
Ledoux, P. 1947, ApJ, 105, 305
Mabuchi, J., Masada, Y., & Kageyama, A. 2015, ApJ, 806, 10
Masada, Y. 2011, MNRAS, 411, L26
Masada, Y., & Sano, T. 2014, ApJL, 794, L6
Masada, Y., Sano, T., & Shibata, K. 2007, ApJ, 655, 447
Masada, Y., Takiwaki, T., Kotake, K., et al. 2012, ApJ, 759, 110
Masada, Y., Takiwaki, T., & Kotake, K. 2015, ApJL, 798, L22
Masada, Y., Yamada, K., & Kageyama, A. 2013, ApJ, 778, 11
Miesch, M. S. 2005, LRSP, 2, 1
Miesch, M. S., & Toomre, J. 2009, AnRFM, 41, 317
Miesch, M. S., Brun, A. S., & Toomre, J. 2006, ApJ, 641, 618
Moffatt, H. K. 1978, Magnetic Field Generation in Electrically Conducting Fluids (Cambridge: Cambridge Univ. Press)
Morozova, V., Radice, D., Burrows, A., et al. 2018, ApJ, 861, 10
Nagakura, H., Burrows, A., Radice, D., et al. 2020, MNRAS, 492, 5764
Nordlund, Å., Galsgaard, K., Stein, R. F., et al. 1994, in Proc. of the NATO Advanced Research Workshop, ed. R. J. Rutten & J. S. Carolus, 471
Ott, C. D., Burrows, A., Thompson, T. A., et al. 2006, ApJS, 164, 130
Parker, E. N. 1955, ApJ, 122, 293
Pedlosky, J. 1982, Geophysical Fluid Dynamics (Berlin: Springer)
Pons, J. A., Reddy, S., Prakash, M., et al. 1999, ApJ, 513, 780
Racine, É., Charbonneau, P., Ghizaru, M., et al. 2011, ApJ, 735, 46
Raynaud, R., Guilet, J., Janka, T., & Gastine, T. 2020, SciA, 6, eaay2732
Rheinhardt, M., & Geppert, U. 2005, A&A, 435, 201
Roberts, L. F., Shen, G., Cirigliano, V., et al. 2012, PhRvL, 108, 061103
Ruderman, M. 1972, ARA&A, 10, 427
Ruderman, M. A., & Sutherland, P. G. 1973, NPhS, 246, 93
Sano, T., Inutsuka, S., & Miyama, S. M. 1999, in Proc. of the Int. Conf. on Numerical Astrophysics 1998 (NAP98), ed. S. M. Miyama, K. Tomisaka, & T. Hanawa (Boston, MA: Kluwer), 383
Scheck, L., Kifonidis, K., Janka, H.-T., et al. 2006, A&A, 457, 963
Schekochihin, A. A., Cowley, S. C., Taylor, S. F., et al. 2004, ApJ, 612, 276
Schrijver, C. J., & Siscoe, G. L. (ed.) 2010, Heliophysics: Evolving Solar Activity and the Climates of Space and Earth (London: Cambridge Univ. Press)
Soker, N. 2020, RAA, 20, 024
Spruit, H. C. 2008, in AIP Conf. Proc. 391, 40 Years of Pulsars: Millisecond Pulsars, Magnetars and More, ed. A. Cumming (Melville, NY: AIP), 391
Steenbeck, M., & Krause, F. 1969, AN, 291, 49
Thompson, C., & Duncan, R. C. 1993, ApJ, 408, 194
Torres-Forné, A., Cerdá-Durán, P., Passamonti, A., et al. 2018, MNRAS, 474, 5272
Torres-Forné, A., Cerdá-Durán, P., Passamonti, A., et al. 2019, MNRAS, 482, 3967
Turolla, R., Zane, S., & Watts, A. L. 2015, RPPh, 78, 116901
Yadav, R. K., Christensen, U. R., Wolk, S. J., et al. 2016, ApJL, 833, L28